Tapered Nonlinear Vibration Energy Harvester for Powering Internet of Things

Kankana Paul[1], Andreas Amann[2], Saibal Roy[1,3, a)]

[1]*Micro-Nano-systems Center, Tyndall National Institute, Lee Maltings, Dyke Parade, Cork, Ireland*
[2]*School of Mathematical Science, University College Cork, Cork, Ireland*
[3]*Department of Physics, University College Cork, Cork, Ireland*
[a)] *Email: saibal.roy@tyndall.ie*

Corresponding author:
Saibal Roy, Tyndall National Institute, University College Cork,
Address: Lee Maltings, Dyke parade, Cork, Ireland, T12 R5CP, Phone: (0) 21234 6331,
Email: saibal.roy@tyndall.ie

Abstract

The lack of a sustainable power source to substitute batteries for long-term applications limits the widespread deployment of wireless sensor nodes in this era of the Internet of Things. Conventional linear Vibration Energy Harvesters are inefficient in converting ambient mechanical energy into usable electrical energy owing to their narrow frequency bandwidth when harnessing mechanical energy that is spread over a wide range of frequencies. In this work, we design, develop and demonstrate high power density nonlinear wideband energy harvesters using novel tapered spring architectures in an autonomous wireless sensor node system. These spring structures exhibit a nonlinear restoring force arising from the atypical stress distribution that can be additionally tuned by changing the taper-ratio in the structure. We investigate different tapering designs in order to achieve optimal spring hardening nonlinearities. This nonlinearity aids in widening the operable bandwidth, making the harvesters suitable for scavenging energy from real-world broadband vibrations. We obtain power densities of the order of $2660\mu W/cm^3g^2$ in the nonlinear energy harvester, outpacing most contemporary energy scavengers. We present a modified Perturb and Observe algorithm that allows tracing of the maximum power point in the context of non-stationary vibration conditions. We use the fabricated nonlinear device to power a wireless sensor node that reports on vital physical parameters (humidity, temperature), thereby enabling a resilient remote data acquisition system. This demonstrates the potential of our design to provide a sustainable energy source for platforms within the Internet of Things.

Key words

Self-powered WSN, Tapered Vibration Energy Harvester, Electromagnetic Transduction, Broadband, Power Density, Maximum Power Point

Introduction The development of low power electronics and the idea of the Internet of Things (IoT) has given rise to the paradigm of the autonomous Wireless Sensor Network (WSN). This facilitates sensing through numerous deployed sensor nodes, complex computations and finally communication of a large volume of data to an external server or user. Such versatile sensor networks have been deployed in healthcare [1], transportation [2], structural monitoring [3] environmental monitoring [4] and security systems [5] creating a smart and responsive environment around us. For example, in the context of continuous condition monitoring of food and medicinal products (temperature and humidity) during transport, a resilient WSN could provide a new level of quality control. However, the widespread diffusion of the sensor nodes is severely restricted by the requirement of onboard bulky power supplies. These power supplies, such as batteries, require substantial installation and maintenance costs [6]. Consequently, the trend of developing battery-less microsystems for wireless sensor nodes has created a burgeoning demand for the

implementation of ambient vibration energy harvesters (VEHs) as a replacement for batteries [7-9] due to the ubiquity and abundance of mechanical energy in the urban environment.

The majority of the reported VEHs involve a linear spring-mass resonator architecture which offers a narrow bandwidth of operational frequencies. This is suitable for narrowband and stationary excitations [10, 11]. However, real-world vibration may possess a broadband spectrum with one or more peaks which may change in amplitude or frequency over time. Hence, there has been substantial research to develop strategies to broaden the operable frequency range of the VEHs. Kim et al. reported a two degree-of-freedom VEH which is designed to extract and convert the mechanical energy both from translational and rotational motion [12]. Owing to the multiple resonant peaks arising from the different degrees-of-freedom, it exhibits a substantially increased frequency bandwidth compared to traditional single degree-of-freedom system. Song et al. designed an array of magnetically coupled piezoelectric beams possessing gradually varying resonant frequencies, which helped in transducing the mechanical energy into electrical energy over a broader frequency range [13]. Arrangements of external magnets have also been used to facilitate bidirectional frequency tuning by exploiting the attractive and repulsive forces between the magnets [14]. Zhao et al. presented an aeroelastic VEH [15] which extracts and converts energy both from mechanical vibrations and wind flow. The mechanical stopper integrated with this harvester aids in broadening the operable bandwidth by coupling the excitation frequencies coming from wind flow and external vibrations. Despite all the above-mentioned strategies, the additional beams, stoppers and external magnets increase the overall footprint of the device which restricts its practical applicability. Therefore, a simple but efficient method to increase the bandwidth of VEHs by using nonlinear spring structures has been recently investigated [16]. This allows for the design of a suitable potential profile [17, 18] which is capable of harvesting energy over a desired frequency range, while maintaining a small footprint. Monostable [19-22] and bi-stable [23-26] oscillators are commonly used for energy harvesting exhibiting single and double potential wells respectively. Here we focus on the monostable variant which offers dynamic flexibility that helps in tuning the overall harvester performance along with simplicity in implementation [27, 28].

The monostable nonlinearity has been incorporated into the energy harvesters by means of magnetic interaction [29, 30]. However, in these structures, the prerequisite of external magnets adds complexity to its implementation. The impetus towards maximizing the scavenged energy output from a small footprint (similar to that of a sensor node) has driven the research towards enhancing the performance of the VEH by modifying the associated geometries. Clamped-Clamped and Clamped-guided spring architecture have been widely used in the field of nonlinear vibration energy harvesting. Electromagnetic [20] and piezoelectric [19] transduction mechanism have both been used, in which the nonlinearity arises from the cubic restoring force associated with the stretching of the thin spring arms as a consequence of large deformation. However, the degree of nonlinearity mostly relying on the thickness of the thin suspension structure leaves very little scope for alteration of the same with small geometrical manipulation without compromising the structural stability. Over the past decade, linearly and exponentially tapered cantilever structures have been widely employed [31, 32] for the implementation of piezoelectric vibration energy harvesters. This type of geometry offers the unique liberty of tailoring and optimizing the length to base width ratio and the degree of tapering [33] to control the stress distribution which improves the performance of the harvester. Combining the advantage of both the geometrical manoeuvring approach, in this work we employ tapered fixed-guided spring structures that demonstrate a strong nonlinear restoring force arising from stretching in addition to bending at a high amplitude of oscillation. The tapering in the spring architecture additionally allows for tuning the degree of nonlinearity by utilizing the atypical stress distribution of such geometrical structures. This enhances the power density of the VEH substantially when compared to the traditional system. The objective of this work is to explore the potential of tapered nonlinear vibration energy harvesters as a sustainable source of energy for powering the WSNs, which are indispensable component of the IoT platform.

In this paper, we investigate the performance of two such Electromagnetic Vibration Energy Harvester (EM-VEH) employing FR4 (Flame Retardant 4) based tapered spring structures. A novel geometry is used to include a stretching-strain based spring hardening nonlinearity into the vibration energy harvesting system. Section 2 outlines the design considerations and fabrication of the harvester prototypes P1 (two tapered spring arms) and P2 (four tapered spring arms). The open circuit and the load performance of the harvesters are evaluated and discussed in Section 3, along with a comparison of their performance with devices previously reported in the literature. Section 4 deals with the development of a complete vibration energy harvesting system. In this section we investigate the Maximum Power Point Tracking (MPPT) of such nonlinear energy harvesters. Lastly, we demonstrate the powering of a Wireless Sensor Node (Cypress IoT kit) through one of the fabricated harvester prototype which could potentially open the path for the implementation of a battery-less WSN for perpetual condition monitoring in a wide range of different applications.

For example, the food and pharmaceutical industry demands a continuous monitoring of the product quality during transport, which could be enabled through such a device.

2. Modelling and Fabrication of the EM-VEHs:

2.1 Design and Fabrication of the EM-VEHs

The alteration of the degree of nonlinearity in the conventional fixed-guided spring architecture is difficult because it depends critically on the thickness of the spring arms [20]. Moreover, the frail link to the load end in these structures allow additional degrees of freedom associated with torsion and rotation, as well as the desired out-of-plane movement. When subjected to a large amplitude of vibration, the thin springs are prone to get damaged owing to these motion. In this context, the trapezoidal spring structure opens up the scope for easy alteration of the strain and stress distribution by modifying the proportion of tapering. These architectures not only offer easier alteration of the degree of nonlinearity as compared with the traditional springs, but also the broad fixed ends of the trapezoidal section help in restricting the additional degrees of freedom of motion.

At the outset of this section, we will demonstrate how the degree of tapering influences the stress distribution in a fixed-guided spring architecture and later we will evaluate the performance of two nonlinear VEH prototypes which employs a set of tapered spring arms. Fig.1 shows four different spring architectures where the tapering of spring arms has been gradually increased. The width of the spring arm reduces linearly towards the load end with a rate $\delta = (w_1 - w_2)/L_1$ where, w_1 and w_2 are the width of the trapezoidal section at the fixed end and the load end respectively. In the structure, L_1 and L_3 are the length of the tapered section, L_2 is the width of the central stage holding the mass. The width of the spring at a point can be then expressed as-

$$w(x) = \begin{cases} w_1 - \delta x, 0 \le x \le L_1 \\ w_1 - \delta(L_1 + L_2 + L_3 - x), (L_1 + L_2) \le x \le L_1 + L_2 + L_3 \\ w_2, L_1 \le x \le L_1 + L_2 \end{cases}$$

The degree of tapering plays an important role in influencing the aerodynamical behaviour of aircraft wings. Generally the proportion of taper in such a structure is quantified as the taper ratio [34], which is the ratio of the length of the tip to the base of the wing. We have employed the taper ratio as the parameter to quantify the degree of tapering and to study its effect on the stress distribution of the spring under consideration.

$$Taper\ ratio = \beta = \frac{w_2}{w_1}$$

In this study, we have considered four different spring architectures, where the taper ratio is gradually decreased from 1 to 0.17 keeping the length of the broad end, and the total length of the springs fixed. The spring has a thickness of 0.25mm. We employed the Solid Mechanics physics interface with the Structural Mechanics module of COMSOL multiphysics to find the stress distribution along the length of the springs and to study the variation of the displacement with the applied force for each of the tapered structure. The springs are fixed at the broader end and the rest of the structure is allowed to vibrate on external excitation. A boundary load is applied to the mass attached to the central part of the spring. We have used a 'user-controlled mesh' with maximum and minimum element size of 3.5mm and 0.63mm respectively, and the maximum element growth rate was 1.5. First we employed a stationary study and included the 'geometric nonlinearity' to find the stress distribution along the line of symmetry of the spring structure as shown in Fig. 1. Subjected to similar load conditions, the stress rises steeply with increased tapering of the spring at the load end for out-of-plane motion. Fig.1(f) reveals the variation of the stress distribution along the line of symmetry of each architecture. The narrow beam width at the load end enhances the stress (force per unit area) as compared to the rectangular spring. To show the effect of tapering on the degree of nonlinearity, we used the parametric sweep tool to apply a varying load to the structure and recorded the corresponding displacement of the tapered end. Fig. 1(e) reveals the relation between the displacement and the applied force which appears due to the combined effect of bending and stretching of the spring. Up to 0.2mm of deflection the spring stiffness is approximately linear, beyond this the nonlinear nature of the spring stiffness comes into play. The degree of nonlinearity enhances as the taper-ratio is gradually reduced. The atypical stress distribution along with the low thickness of the springs aids in inducing such nonlinear restoring force into the system.

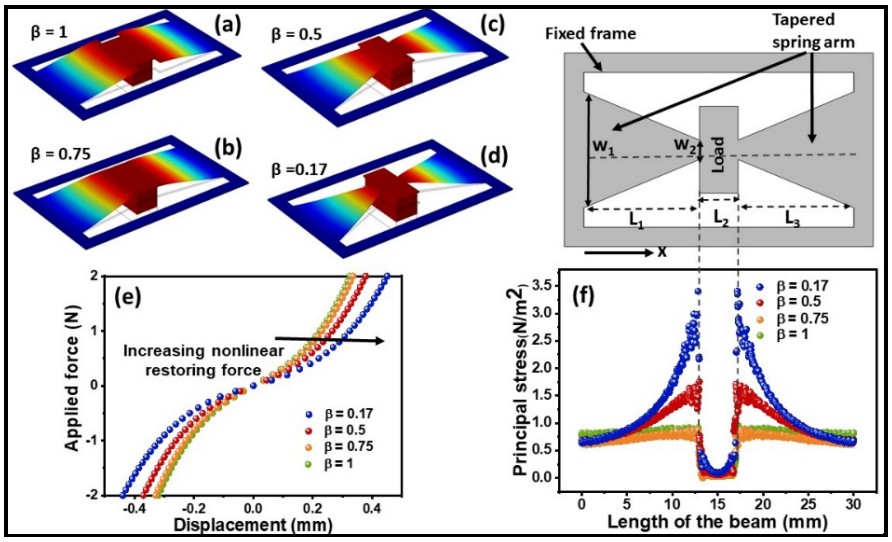

Figure 1: Tapered FR4 spring architecture with spring arms having (a) 1 (b) 0.75 (c) 0.5 (d) 0.17 taper ratio and the variation of their (e) nonlinear restoring force, (f) principal stress distribution along the length of the beam is shown.

Two VEH prototypes have been designed to exploit this atypical stress distribution, which could potentially induce the stretching based strain when the spring vibrates and undergoes large deflection in the out-of-plane motion. The detailed schematic of both the prototypes is shown in Fig.2. Structure P1 has dimensions 35mm × 19mm × 0.25mm and the structure P2 has 38mm × 26.3mm × 0.25mm. Both structures are fixed at the outer frame and the rest of it is free to move on vibration (Fig. 4). A central stage (8.3mm × 10.4mm) which is dedicated for the assembly of the magnets is held by a couple of slotted tapered spring structure in P1 (each has broad end 8.6 mm and the narrow end 4.3mm) and four such springs are used in P2. The taper-ratio of 0.5 has been used here by optimizing the structural stability and the desired out-of-plane modes of vibrations within the low frequency range. A slot 8mm × 2mm is left at the centre for the vertical arrangement of the coil. the two spring structures have been laser micro-machined on 250µm thick FR4 sheets. FR4 is a grade of 'Flame retardant' low-cost anisotropic material which is popularly used in printed circuit boards. It has been used as the material for the fabrication of the nonlinear spring structures owing to its low Young's modulus (typically 22GPa) that aids in reducing the frequency of oscillation of the device making it more efficient in scavenging a significant fraction of the mechanical energy which is distributed mostly in the low frequency domain [35].

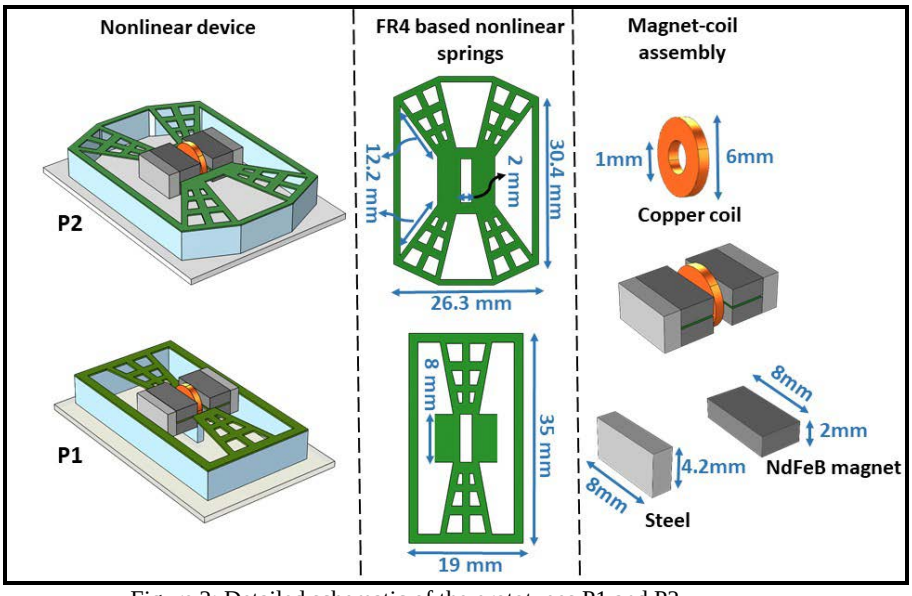

Figure 2: Detailed schematic of the prototypes P1 and P2.

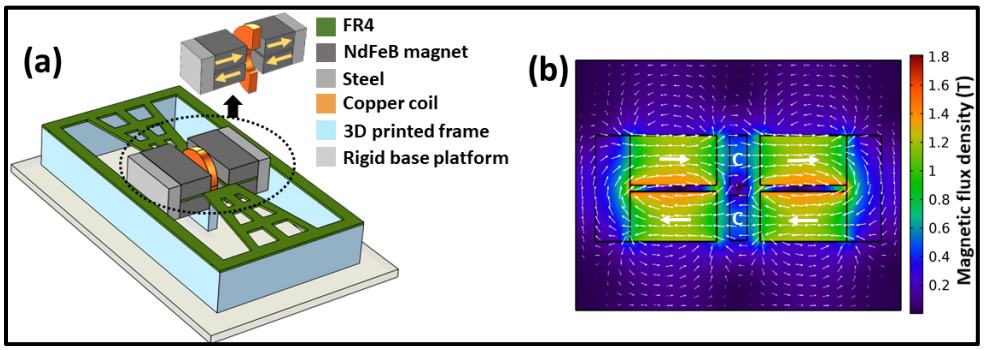

Figure 3: (a) Schematic of the prototype P1, (b) Schematic and direction of magnetization in the coil-magnet assembly of P1.

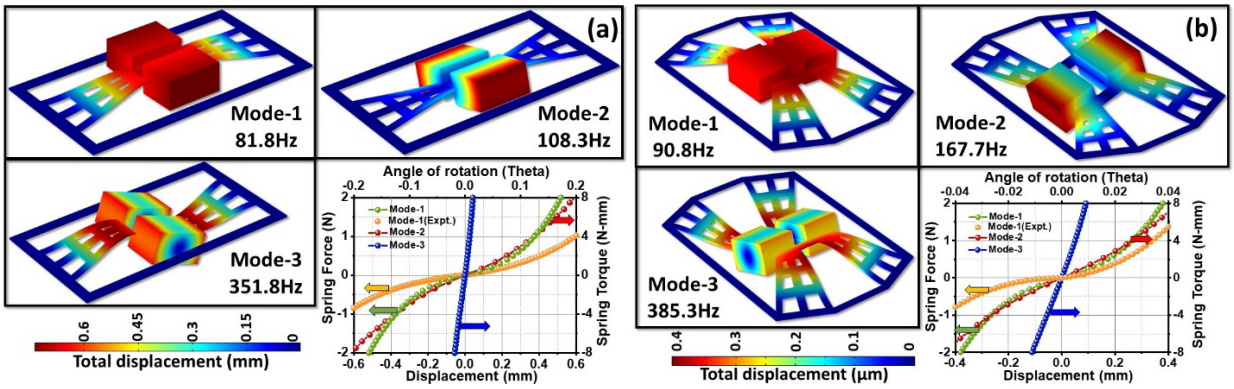

Figure 4: Finite element analysis of the spring structures depicting different modes of P1 (a) and P2 (b). The variation of the spring force with the amplitude of displacement corresponding to mode-1 and the variation of spring torque with angle of rotation corresponding to mode-2, 3 have been shown. Experimentally obtained force-displacement corresponding to Mode-1 is shown (in orange).

The magnet assembly comprises four high energy density sintered NdFeB N50 (8mm × 4mm × 2mm) magnets along with a couple of soft magnetic (steel keeper) blocks (8mm × 4.2mm × 1.6mm) arranged to create a closed magnetic flux path intensifying the flux density in a precise location [10] (Fig. 3). They are epoxy bonded to the central platform of P1 and P2 which is specifically designed for them. The enamelled wire-wound copper coils of 1mm inner diameter, 6mm outer diameter and 2500 turns, have been fixed vertically to the base platform through a rigid 3D printed structure. The resistance of coils used with P1 and P2 is 1022Ω and 1046Ω, respectively. The electromagnetic interaction due to the out-of-the-plane displacement of the moving magnets with respect to the static coil has been studied with Ansys Maxwell finite element analysis tool. The resulting values of the electromagnetic coupling coefficient (γ) are 14.1Wb/m and 14.3Wb/m for P1 and P2 respectively.

The Solid Mechanics interface of the COMSOL Multiphysics platform has been used to perform finite element analysis of the conceived energy harvester units. The first few eigen-modes of P1 are at 81Hz, 108Hz and 351Hz, where the first one is responsible for the out-of-plane motion, and the latter two corresponds to the sideways tilt and flip respectively (Fig. 4(a)). The first few eigen-modes for P2 at 90Hz, 167Hz and 385Hz (Fig.4(b)) demonstrate similar dynamics to P1. Under small displacement the restoring force of these springs mostly reflect the bending of the structures, until the displacement exceeds the thickness of beams. Beyond this displacement it shows stretching induced nonlinear behaviour and the spring stiffness involves both bending and stretching components. The resulting nonlinearity is portrayed in Fig.4 for the first two modes. Fig. 4(a) and (b) also presents the experimentally obtained force-displacement relationship of the FR4 spring structures, the details of the experiment and further analysis is presented in section 3.1. The linear (k) and nonlinear (k_n) spring stiffness coefficient obtained from the stationary analysis of the 0.25mm thick structures P1 and P2 are 1298 N/m and 10×10^9 N/m^3, 2130 N/m and 21×10^9 N/m^3

respectively. The degree of nonlinearity could be further enhanced by reducing the thickness of the structure, allowing a higher amplitude of displacement, but the stationary analysis reveals structural instabilities owing to the gravitational pull for lower thickness of FR4 spring structures. Hence, the optimized thickness of 0.25mm has been chosen in this case to bring nonlinear effects into the system without compromising the structural stability.

2.2 Dynamical analysis

The governing equation of the electromechanical oscillator that exhibits electromagnetic transduction can be approximated by [26, 36],

$$m\ddot{x} + c_m\,\dot{x} + \frac{\partial U(x)}{\partial x} + \gamma I = -m\ddot{z}$$

where, m is the mass of the system, c_m is the mechanical damping factor, $\frac{\partial U(x)}{\partial x}$ is the total spring force associated with the system, I is the induced current in the coil and γ is the electromagnetic coupling factor. The system is subjected to an external excitation $\ddot{z}$ causing displacement of the form $z = Z_0\,sin(\omega t)$.

In this work we are considering a monostable oscillator with Duffing potential $U(x)$ that involves the energy stored in the spring due to bending $U_b(x) = \frac{1}{2}kx^2$ and stretching $U_s(x) = \frac{1}{4}k_n x^4$, where, k and k_n are the linear and non-linear spring stiffness coefficients. The electrical energy is extracted across a suitable load (resistive) R_L, then the external conversion circuit involving the coil resistance R_c, inductance L can be modelled using Kirchhoff's voltage law as,

$$L\dot{I} + (R_c + R_L)I = \gamma\dot{x}$$

Neglecting the effect of L at low frequencies and using the equations above, the electrodynamical representation of the oscillator takes the form,

$$m\ddot{x} + \left(2m\rho\omega + \frac{\gamma^2}{R_c + R_L}\right)\dot{x} + kx + k_n x^3 = m\omega^2 Z_0 \sin(\omega t)$$

where, ρ is the mechanical damping coefficient. This equation has been numerically solved using fourth-order Runge-Kutta method using mathematical tools of MATLAB to find the voltage and power in the open-circuit (Fig. 6(c) and (d)) and closed-circuit (Fig. 7(c) and (d)) form. The results are compared with the experimental findings and are explained in the Experimental Methods, Results and Discussion section.

3. Experimental Methods, Results and Discussion:

3.1 Spring stiffness measurements

To experimentally verify the force-displacement relationship of the fabricated FR4 springs, we have used the mechanical test system 'Instron 5565' (Fig.5) and subjected the devices to compressive load. The test set-up consists of a load frame that holds the crosshead which moves up or down when tensile or compressive load is applied on the specimen. For this test we used a load cell that is capable of delivering up to 500N compressive force on the device under test through the attached fixtures. The load cell converts the measured load into electrical signal and the Bluehill software linked with Instron displays this load along with the corresponding displacement. To ensure better accuracy, the load frame is displaced at a slow speed of 1mm/min. Since we have only used this set-up for compressive loads, to emulate the effect of the tensile force on the device, we have subjected the opposite side of the device to similar compressive load condition. The obtained force-displacement considering the out-of-plane movement of the FR4 springs has been shown in Fig. 4(a) and (b). The linear and nonlinear spring stiffness coefficient are 705.5N/m, 2.5×10^9N/m^{3}and 775.8N/m, 13.1×10^9N/m^{3}for P1 and P2 respectively. The discrepancy between the experimental data and those obtained from the model can be attributed to the following factors. First, in the model we have considered

nominal thickness of 0.25mm of the FR4 springs, whereas in practice there is a possibility of thickness variation in the FR4 sheet. Second, the anisotropic nature of the FR4 material is not taken into account in the model which would have reasonable effect on the spring stiffness. Third, the experimentally obtained value of the linear spring stiffness coefficient is lower than those of the model. This is due to the fact that, the structures with which the FR4 springs are fixed to the base platform are considered to have infinite stiffness in the model but in practical application the 3D printed fixtures are not infinitely rigid. The stiffness coefficients are employed in the dynamical model to predict the frequency response of the system in both the closed and open circuit condition.

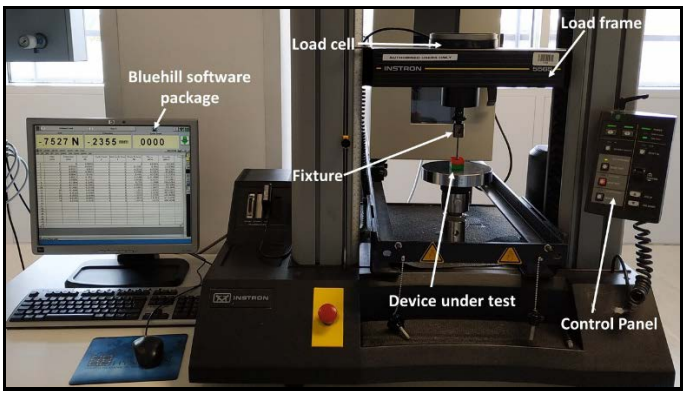

Figure 5: The Instron test set-up for the measurement of force-displacement relationship of the FR4 spring structure.

3.2 Open Circuit condition

For a relatively lower level of acceleration such as 0.1g, the response from both of the system P1 and P2 is nearly resonant in nature as the response is almost identical irrespective of whether the frequency is swept in the forward or in the reverse direction (resonant frequency 70Hz and 74Hz for P1 and P2 respectively). From the COMSOL modelling, the first few eigen modes of P1 are at 81Hz, 108Hz and 351Hz and that of P2 are at 90Hz, 167Hz and 385Hz. In both cases, the experimental values of the natural frequencies of oscillation are lower than that obtained from COMSOL. The 3D printed structures, which fix these spring structures to the shaker plate in the experiments does not possess infinite stiffness as it does in case of the finite element analysis. This lowers the value of the spring stiffness and pulls down the frequency of vibration in contrast to those obtained from the finite element analysis. With the increasing amplitude of external excitation, the response of both system becomes gradually non resonant (Fig. 6(a) and (b)). As the axial strain on the spring structure builds up forcing it to stretch, the oscillators start exhibiting complex nonlinear dynamic behaviour, for example the jump phenomena. When the system is subjected to a harmonic excitation with slowly varying frequency, the response from the system jumps either up (broken line) or down (solid line) at a certain frequency also termed as the saddle node point. This non-resonant nature and the multistability aids in enhancing the bandwidth of operation significantly as compared with its linear counterpart.

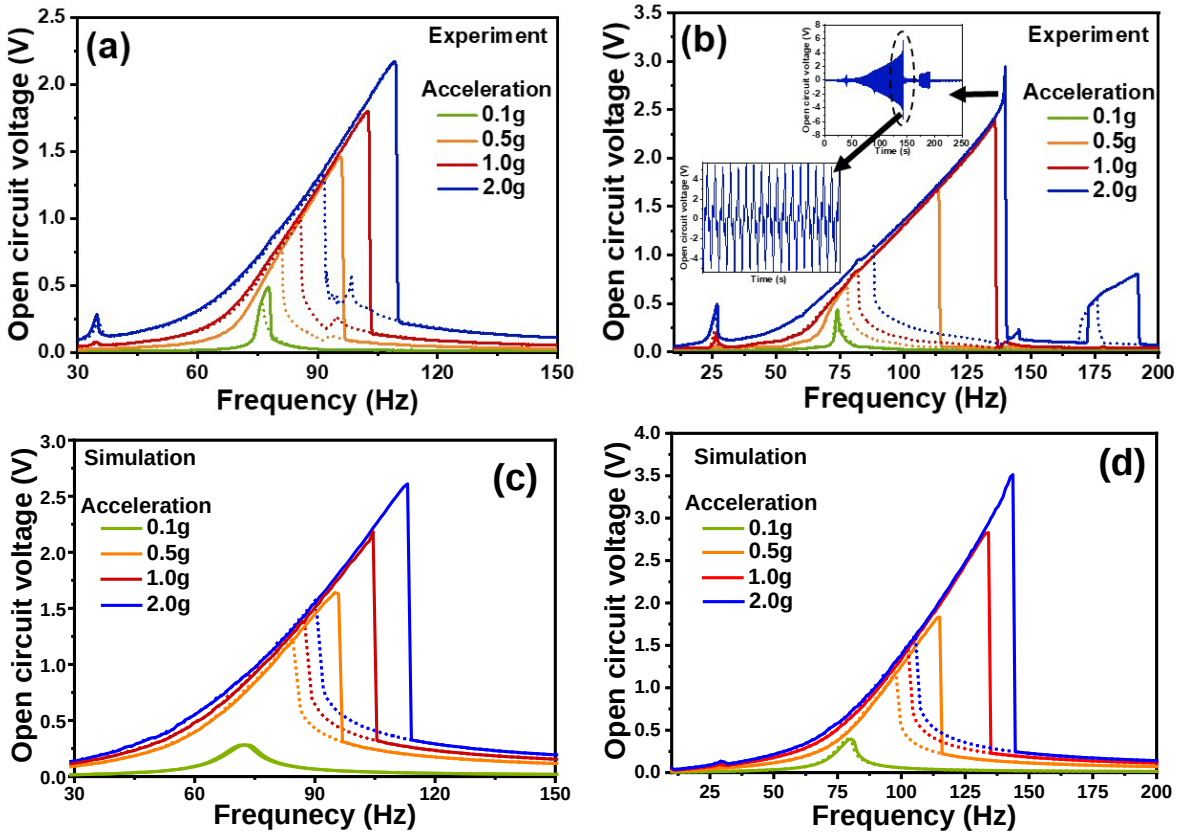

Figure 6: (a) The open circuit voltage measurement of the prototype P1. (b) The open circuit voltage measurement of the prototype P2. Time domain signal at the inset the portrays the peculiar sharp peak of the open circuit voltage at 2g. The simulated results are shown in (c) and (d) for the prototype P1 and P2 respectively.

For P1, the peak open circuit voltage at 0.1g is 0.5V which increases to 2.2V at 2g acceleration level. In addition to this, an additional relatively smaller peak is observed at 34Hz at higher amplitudes of the external driving force which can be attributed to the activation of super-harmonics [37, 38] at almost half of the fundamental frequency of vibration of P1 (Fig. 6(a)). This bears the characteristics of nonlinear dynamical systems such as Duffing oscillators that allow the extraction of significant amount of vibrational energy even from comparatively lower frequency. In the reverse sweep of the open circuit voltage for P1, an additional peak is noticed at 98Hz which could be due to the adjacent eigen modes, mostly responsible for titling motion as found in the finite element analysis. In the forward sweep there is no such trace found which indicates that this is a highly damped oscillation mode. Initially the shaker plate excites only excites the modes responsible for the out-of-plane motion, at a higher level of acceleration the sufficient mechanical energy fed into the system also excites the other associated modes.

The open circuit voltage is found to ramp up from 0.4V at 0.1g acceleration to 2.9V at 1g acceleration for the P2 prototype. At the higher external excitation level, a voltage peak arising from a super-harmonic component is observed at 27Hz, almost at 1/3rd of the fundamental frequency of oscillation (74Hz). A peculiar trend is noticed in the higher excitation amplitude regime where, with increasing the acceleration from 1g to 2g, the peak voltages increased from 2.4V to 2.9V without any significant bandwidth enhancement (inset of Fig. 6(b)). The emergence of an additional nonlinear mode at higher frequency around 175Hz is observed which accounts for the wobbles and instabilities in the structure at the higher forcing amplitude. This additional mode strengthens with higher acceleration by drawing significant amount of power from the primary nonlinear mode. This is why, despite feeding substantial energy through forcing, the peak voltage or the bandwidth of the primary mode doesn't enhance as expected. It indicates the possibility of coupling between these two adjacent modes that are exchanging energy between each other. Fig. 6(c) and (d) depicts that there is good qualitative agreement between the experimental results and the results obtained through numerical modelling as explained in the previous section. However, the 'jump' frequencies slightly differ as the two results are compared quantitatively. For example, with 2g acceleration amplitude, the response jumps

from the high energy branch to the low energy branch at 109Hz for P1, whereas numerically that point shifts to 113Hz. Similarly, for P2 the jump frequency obtained from the model is 144Hz, whereas experimentally the jump occurs at 139Hz at 2g acceleration. This can be due to the energy dissipation that takes place due to the effect of stretching, which is not taken into account in the numerical modelling. Also, the additional modes that are experimentally observed at 98Hz and 175Hz for P1 and P2 respectively, are not reproduced in the numerical results. This disparity can be attributed to the fact that we consider only one degree of freedom for modelling, whereas in reality the complex 3D system possesses additional degrees of freedom. In addition to this, the open circuit voltage as obtained through the model is also higher than what has been experimentally observed. This can be explained by considering the damping. In the model we only consider the damping which is proportional to the velocity of movement of the spring, whereas the damping experienced by the device in real-world can have more complex dependency on the velocity.

3.2 Load performance

In the next part of the experiment, the output voltage is measured for both of the fabricated prototypes P1 and P2 at a fixed level of acceleration of 0.5g across variable load resistors ranging from 200Ω to 8kΩ. The devices are excited with a predefined sinusoidal vibration close to their peak power frequencies. The peak load power was found to be 550μW across 1.6kΩ load resistance for P1 and 520μW across 1.8kΩ load for P2 with peak load voltages 943mV and 966mV respectively (inset of Fig. 8). Next the effect of the amplitude of external excitation on the load power of the system has been studied experimentally with the optimum load resistance. For P1, the half power bandwidth at 0.1g acceleration is found to be 2.6Hz with a peak load power of only 9.7μW. Upon on escalating the input acceleration, the peak load power increases to 0.63mW for 1g acceleration level resulting in widening of the bandwidth to 10Hz (Fig. 7(a)). Similarly, for P2 the peak load power and the bandwidth at 0.1g acceleration level are 20μW and 1.5Hz which surges to 1.3mW and 23Hz at 1g (Fig. 7(b)). It is interesting to study the bursts of power in the low frequency range in P2 due to the super-harmonics. At around 28Hz for 1g acceleration this mode extracts 9.6μW of electrical power into the load resistance which is significantly higher than the rest of the low frequency range. In addition to this, in the high frequency zone at 178Hz a sudden burst of power of 1.8μW comes from the additional nonlinear mode which has been identified and explained in the open circuit voltage plots as well. The experimentally obtained load characteristics of the device are compared with the numerical results (Fig. 7(c) and (d)). The overall trend of how the system response varies with the change to the excitation amplitude agrees well with the experimental results.

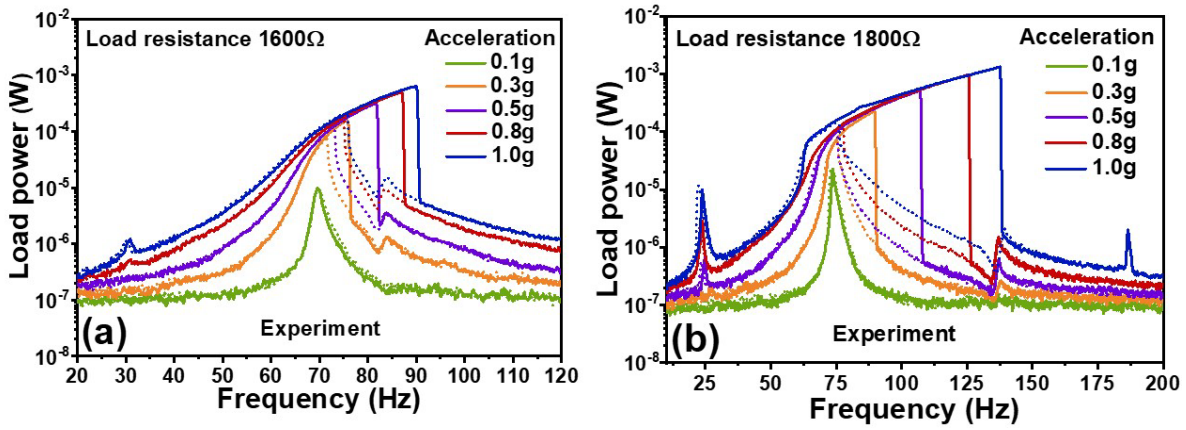

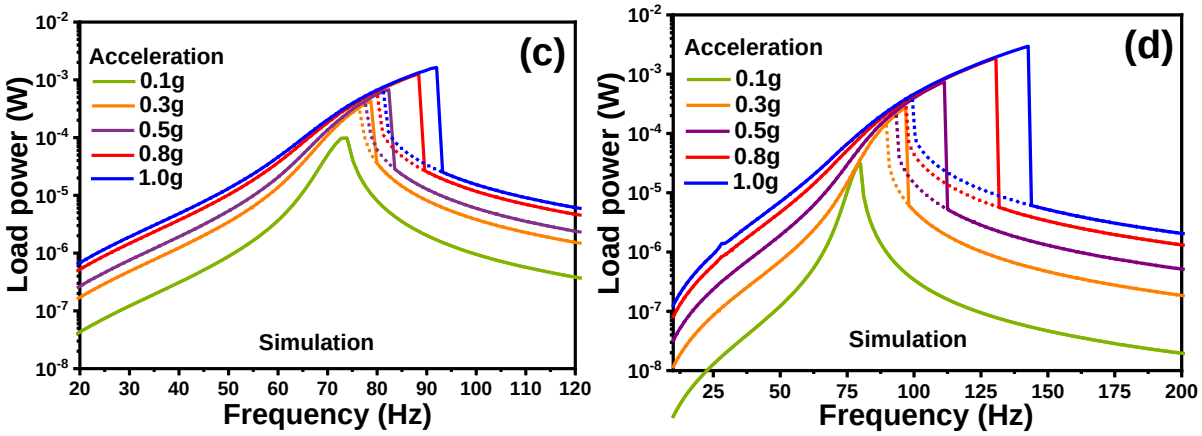

Figure 7: Variation of the load power at optimum load resistance with frequency for the prototype (a) P1 and (b) P2. The simulated results are shown in (c) and (d) for P1 and P2 respectively.

If the optimum load resistance, i.e. the value of load across which maximum output power is obtained is considerably greater than the resistance of the coil employed then it indicates strong electromagnetic coupling between the coil and the magnet resulting in larger electromagnetic flux linkage [39]. The electrical damping [40] associated with the system is dependent on the resistances of the coil (R_c), load (R_L) and on the electromagnetic coupling (γ) between the coil and the magnet. Taking into consideration the significant predominance of the vibrational energy distribution over the low frequency domain (f <200Hz), the effect of coil inductance (ωL) on the electrical damping (C_e) can be neglected as compared with the sum of the coil and load resistance. The damping can be expressed as,

$$C_e = \frac{n^2\left(\frac{d\Phi}{dz}\right)^2}{(R_c + R_L)} = \frac{\gamma^2}{(R_c + R_L)}$$

where,Φ is the magnetic flux linkage, n is the number of coil turns and $n\left(\frac{d\Phi}{dz}\right)$ represents the electromagnetic coupling γ .By increasing the load resistance for a fixed level of external forcing, the electrical damping associated with the system reduces, and this opens up the scope for modulation of the load power response of such nonlinear oscillators just by tailoring the load resistance (Fig. 8). This is possible when the electromagnetic coupling is strong enough so that the electrical damping in the system dominates over the parasitic damping. For 200Ω resistance, the electrical damping gets larger and the peak load power is only 180μW for P1 and 140μW for P2. However, increasing the load resistance to 1600Ω, 3200Ω and eventually to 8000Ω the bandwidth clearly increases but the power doesn't increase continuously. The peak load power reaches a maximum for the optimum load resistance of 1.6kΩ and 1.8kΩ for P1 and P2 respectively. Further increasing the load reduces the electrical damping significantlywhich enhances the operable bandwidth at the cost of reduced peak load power. So this study brings out a clear trade-off between the magnitude of extracted power and the bandwidth of operable frequencies. Hence, the requirements of the target application can be met by altering load resistance, in particular when the electrical/electromagnetic damping associated with the system is dominating over mechanical damping.

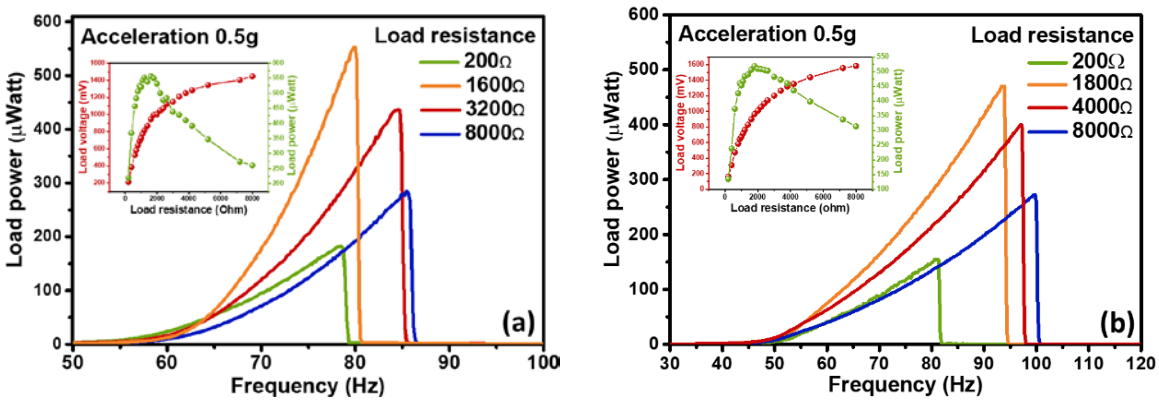

Figure 8: Variation of the load power with load resistance at 0.5g acceleration for P1(left) and P2(right)

The inherent wideband characteristics of the nonlinear oscillators make it easier to compare the different oscillators by considering their bandwidths at half of the peak power points. However, the concept of such bandwidth comparison could be misleading for the nonlinear oscillators as truncating the peak power could eventually lead to bringing the half power point further down and deceptively indicating the enhancement of the bandwidth at that point. However, such an enhancement would be at the cost of compromising the obtainable power from the harvester. Rather, the enhancement of the width of the bi-stable or hysteresis region in this context could be a more reliable parameter to assess the effectiveness of the incorporated nonlinearity in the system. Fig. 9 shows the variation of the hysteresis width of the nonlinear energy harvester units with the amplitude of external excitation at the respective optimum load resistance. The solid line corresponds to the jump-down frequencies and the dotted line represents the jump-up frequencies. At lower acceleration the hysteresis width is quite low for both of the harvesters up to 0.2g which is expected as in this regime the system demonstrates nearly resonant behavior. On further increasing the magnitude of external forcing, the structures experience strain arising from stretching instead of only bending, which makes the restoring force a nonlinear function of the displacement. This in turn widens the hysteresis region dramatically. The jump down frequency shifts toward higher frequency more drastically due to the hardening nonlinearity as opposed to the jump-up frequency which doesn't vary much with respect to the fundamental frequency of oscillation despite of the presence of strong nonlinearity [41]. At 0.2g the 4.5Hz and 4.7Hz hysteresis width increases to 11Hz and 45Hz at 1g for P1 and P2 respectively. The prototype P2, which has a higher degree of nonlinearity clearly shows a wider hysteresis region which enables the system to scavenge the vibrational energy from a broader range of frequencies.

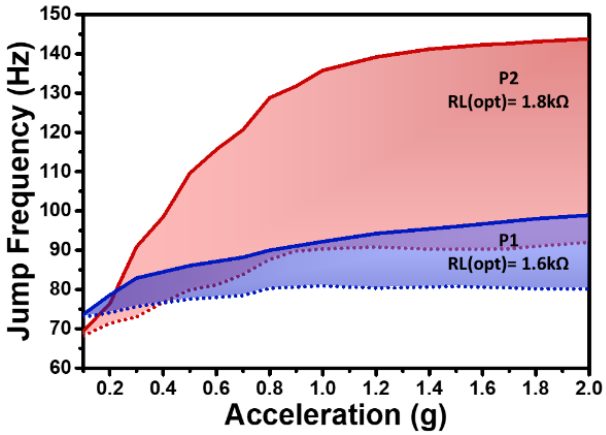

Figure 9: Comparison plot of the variation of hysteresis width of P1 and P2 with external excitation amplitude.

Evaluation of an energy harvester's overall performance is not straight forward, mostly because of the different size, device architecture and the different transduction mechanism used. The performance metrics often fail to express the efficiency of the overall system taking into account all the parameters such as- the device volume, amplitude of external acceleration, frequency of excitation etc. In addition to this, the target requirement also changes. For example, if the application requires resonant VEH, the peak load power is an important scale of performance evaluation for

them as opposed to the bandwidth. On the contrary, if the target application needs an energy scavenger with broader bandwidth, then along with the high power, a wider range of operable frequency becomes an important parameter for harvester performance. Here, we aim to highlight the efficacy of the conceived tapered geometry employed in a nonlinear wideband energy harvester as compared to the conventional device topologies. Table-1 shows the comparison of the device performance on the basis of the operable bandwidth that it offers, and the power density (=peak power/volume. acceleration^2). In calculating the power density for our device, we have considered the overall footprint that the device occupies instead of the volume of the material only. It can be observed that among the meso-scale devices referenced here, our harvester unit produces higher power per unit volume and provides considerably larger bandwidth as well.

TABLE-1
Comparison of contemporary VEH devices with P1 and P2

Reference	Size scale/ Volume (cm^3)	Bandwidth/ operable frequency (Hz)	Power density ($\mu W/cm^3g^2$)
[13]	1.78*	~ 30Hz at 1g	243$\mu W/cm^3g^2$ at 78Hz
[20]	0.78	10Hz at 1g	0.45$\mu W/cm^3g^2$ at 244Hz
[14]	50	22-32 Hz at 0.08g	875$\mu W/cm^3g^2$ ($= \frac{280\mu W}{50cm^3\ 0.08^2g^2}$) around 22-32Hz**
[25]	2.97	Bandwidth increased by 5Hz at 0.5g	~30$\mu W/cm^3g^2$ ($= \frac{7.4\mu W/cm^3}{0.5^2\ g^2}$) at 35Hz**
[22]	6	4.5Hz at 1g	483.3$\mu W/cm^3\ g^2$ ($= \frac{2.9mW}{6cm^3\ 1g^2}$)at 150Hz**
This work, P1	0.83	9Hz at 0.5g 11Hz at 1g	2660$\mu W/cm^3g^2$ ($= \frac{665\mu W/cm^3}{0.5^2\ g^2}$) at 79Hz
This work, P2	1.23	29Hz at 0.5g 45Hz at 1g	1692$\mu W/cm^3g^2$ ($= \frac{423\mu W/cm^3}{0.5^2\ g^2}$)at 106Hz

*considering the proof mass only, ($\frac{\text{Total maximum power output}}{\text{power density}} = \frac{430.7\mu W}{243\mu W/cm^3g^2}$)

**calculated power density

4. Demonstration of complete Energy Harvesting solution:

4.1 Variation of Maximum Power Point for Nonlinear EM-VEH

The growing interest of establishing a robust network of deployed wireless sensor nodes (WSNs) to create a responsive environment around us, while connecting the physical world to the digital world at the user end demands for a sustainable power source to replace the batteries in such nodes. The high efficiency vibration energy harvesters are one of the potential substitute to batteries. However, their performance depends critically on the ambient vibration

conditions [42, 43]. The embedded electronics in the majority of commercially available WSNs typically require 3-3.3V DC voltage to power them up. Hence, to meet the power requirement of the subsequent load circuitry, the AC

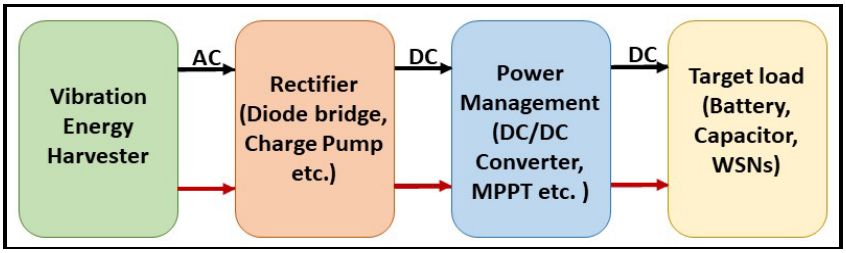

Figure 10: System architecture for powering a target load through ambient Vibrational Energy Harvesting

output of the energy harvester must be rectified. However, this rectified voltage cannot be fed directly to the load as it depends on the excitation amplitude and frequency. Hence, after this AC-DC conversion a suitable DC voltage regulation (DC-DC conversion) is required as a part of an efficient power management approach (Fig. 10). To enhance the extracted energy from such harvesters, it is necessary to dynamically track the point of maximum obtainable power that varies with the vibration frequency and acceleration. The Maximum Power Point Tracking (MPPT) controller is a prevalent component of the power management circuit that alters the duty cycle of the DC-DC converters, allowing the system to look for the voltage corresponding to the maximum electrical power. Various MPPT strategies, mainly for the Photovoltaic (PV) power system have been reported [44-46], for example, Perturb and Observe, Fractional Open Circuit Voltage and Fractional Short Circuit Current etc. Among these, one of the simple approaches is the Perturb and Observe mechanism which involves perturbation of the operation point of the VEH at definite sampling interval while measuring the DC voltage. Furthermore, it checks if the measured voltage is greater or less than that of the previous sample, and accordingly it drives the system either in the same or in the reverse direction to find the MPP. This strategy has been recently used with the resonant electromagnetic vibration energy harvester [47], in which the sampling frequency along with the amplitude of the perturbation duty cycle is tailored to drive the system voltage towards MPP. However, an intelligent MPPT algorithm for the nonlinear energy scavengers, which possess non-identical electromechanical characteristics compared to the conventional resonant harvesters, has not been explored in detail yet.

The following experiment has been performed in order to provide an insight in to the trend of Maximum Power Point variation for Nonlinear VEHs, when subjected to different vibration conditions. The power extracted from the VEH optimizes when the output impedance of the energy harvester matches with that of the interfacing circuitry. The AC output of the harvester prototypes has been rectified employing the Dickson charge pump configuration which is used for rectifying and boosting up the low AC voltage output [48, 49]. Owing to the simple electrical circuit and high efficiencies, this particular configuration is often used with the vibration energy harvesters, enabling it to power the target loads. Hence, a charge-pump interface has been implemented in this case consisting of capacitors C_1 to C_4 each of 1μF and four Zener diodes D_1 to D_4 (Fig. 13). The load resistance connected across the rectifier output has been varied from 200Ω to 10kΩ while the corresponding load voltage is measured and the load power is calculated. For the sake of simplicity, the load in this case has been considered to be resistive unlike the practically available reactive load. For both P1 and P2, this experiment has been performed in two sets, firstly by varying the amplitude of external excitation while keeping the frequency of excitation fixed and well within the hysteresis region (Fig.11(a) and (c)). Secondly, by keeping the amplitude of excitation fixed and varying the frequency of excitation over the hysteresis region while maintaining the oscillator response in the high energy branch (Fig. 11(b) and (d)).

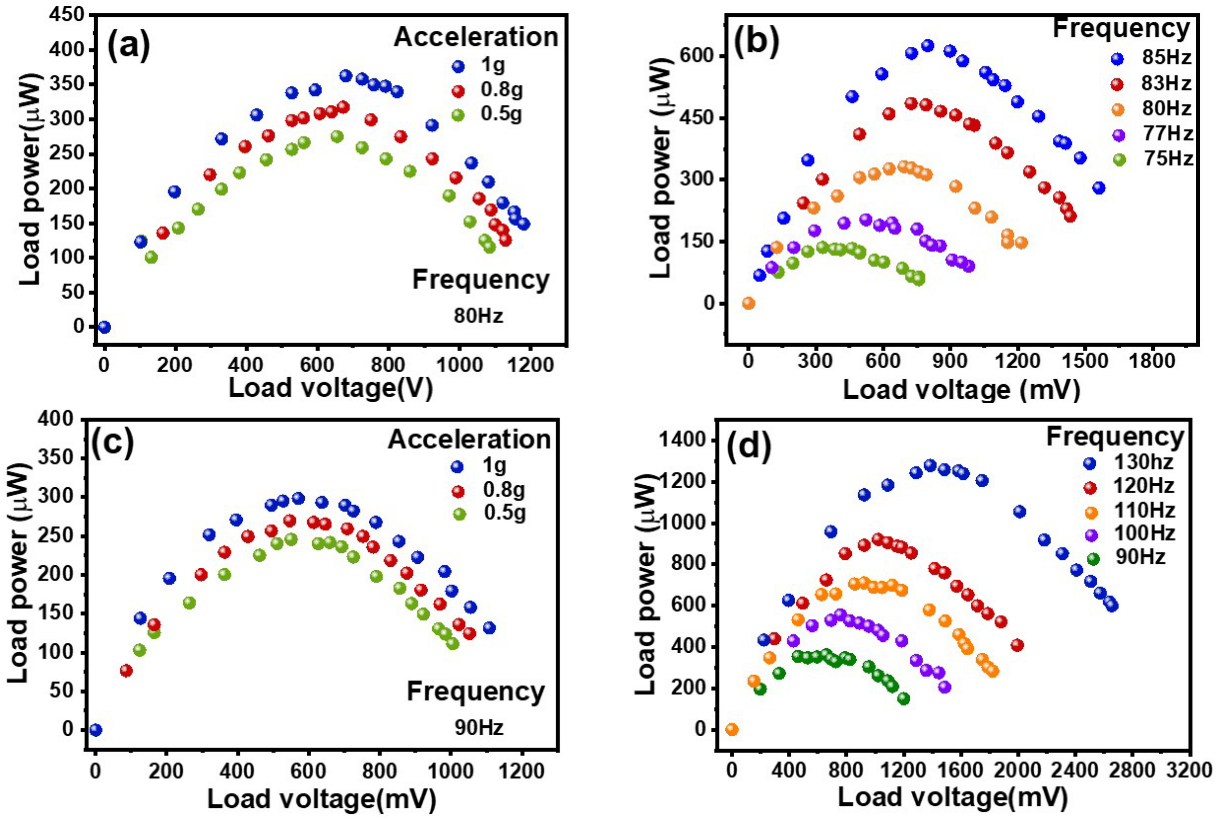

Figure 11: Variation of Load power with respect to load voltage at different level of external acceleration for P1 (a) and P2 (c). Variation of Load power with respect to load voltage at different values of excitation frequency for P1 (b) and P2 (d).

From the load power-voltage characteristics, we can observe that the load power initially increases with increasing load voltage, it attains a maximum value and eventually drops beyond that point with increasing load voltage. The amplitude of the applied force is varied keeping the frequency fixed at 80Hz for P1 and 90Hz for P2. The variation of the load power with the load voltage is shown in Fig. 11(a) and (c). Although the acceleration has been varied from 0.5g to 1g, no significant change either in the optimum power point or the overall variation has been observed as is prominent in a conventional resonant system [47, 50]. This can be explained by the load performance of both the prototypes in Fig.7(a) and (b). As the acceleration is increased, the excess energy pumped into the system at the specified frequencies aid in widening the hysteresis width rather than contributing towards enhancing the peak load power. Hence, in the next set of experiments the amplitude of vibration was fixed at 1g for both the prototypes and the frequency of excitation has been varied over the hysteresis region- 75Hz to 85Hz and 90Hz to 130Hz for P1 and P2 respectively. In Fig.11(b) and (d) the variation of the load power-voltage has been portrayed, while the shift in the variation for different frequencies can be very clearly observed. The maximum power for P1 changes from 327μW to 796μW when the frequency is changed from 75Hz to 85Hz. These results also agree with the load performances (Fig.7) of the devices, where a significant change of load power can be observed over the specified range of frequencies.

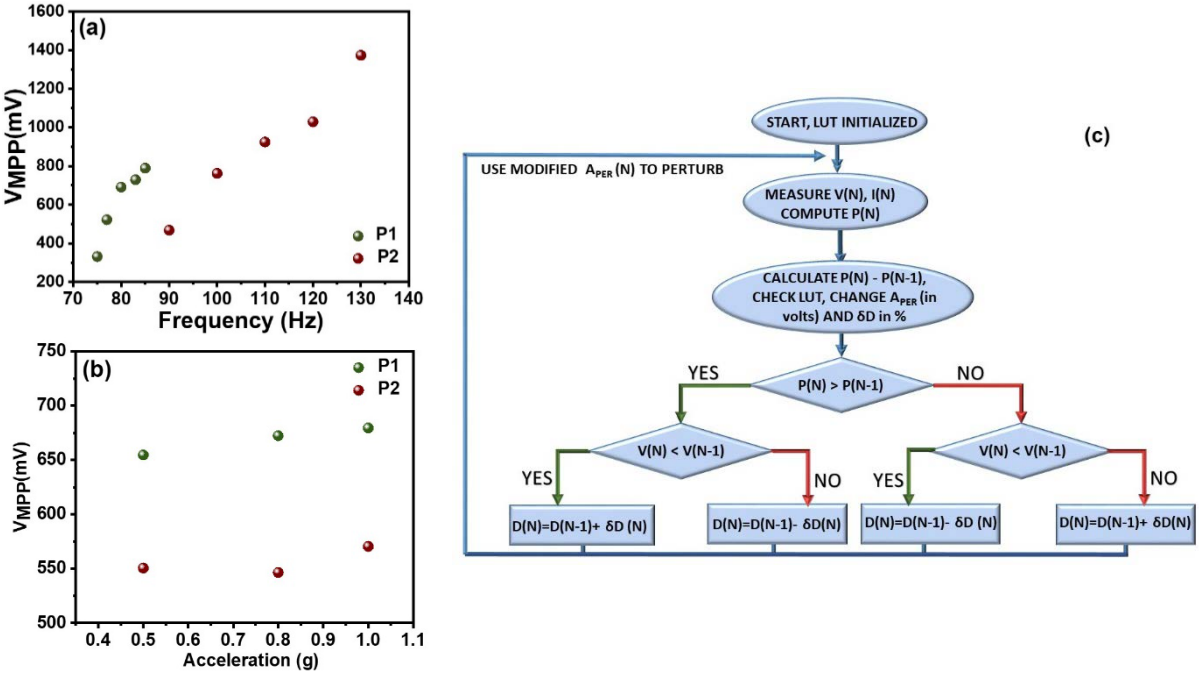

Figure 12: Variation of the DC voltage corresponding to the maximum power point with (a) frequency variation (b) amplitude of external force variation for P1 and P2 as obtained from Fig. 9. The adjacent flow chart (c) depicts the a suitable Perturb and Observe strategy.

The unimodal distribution of the power in Fig. 11 is well suited for employing Perturb and Observe strategy for the tracking of the maximum power point. However, as opposed to the conventional algorithm for the linear VEH, this algorithm would need modification to adapt to a real-world vibration environment and drive the operating point towards MPP. The trend of variation of the DC voltage (V_{MPP}) corresponding to the maximum power point is different when the frequency of operation, or the amplitude of excitation is changed (Fig. 12). At a fixed amplitude of acceleration, the V_{MPP} changes from 331mV to 789mV over a frequency band of 10Hz for P1. However, no significant variation could be noticed in V_{MPP} when the acceleration amplitude is doubled from 0.5g to 1g. Hence the size of the perturbation (A_{PER}) along with the duty cycle (δD) of the DC-DC converter needs to be dynamically adjusted to facilitate the efficient tracking of V_{MPP}. In order to save the system from losing the direction of tracking when it is subjected to fast changing environment, the knowledge of such variation of V_{MPP} as obtained from initial experiments can be conveniently programmed into the MPPT controller in the form of a lookup table (LUT). Once the tracking starts (Fig. 12(c)), following a predefined perturbation, the MPPT controller measures the DC output from the system and computes the power P(N). Furthermore, it computes the change in the obtained power as compared to the last sample and the corresponding DC voltage. Accordingly, the controller modifies the duty cycle D(N) associated with the DC-DC converter until it finds the MPP. Unlike the traditional tracking, at this point the system could check the LUT to find if the change in V_{MPP} corresponds to that of frequency variation or acceleration change. Accordingly, the controller can then assign a suitable A_{PER} and δD to use in the $N+1^{th}$ trial.

The overall performance of such an energy harvesting system relies critically on the individual efficiency of the converter blocks. This requires an accurate MPPT algorithm to optimize the power extraction. This study opens up the scope for development of a suitable MPPT strategy dedicated for such a complex nonlinear system. This will aid in extracting the maximum possible mechanical energy from the harvesters when subjected to real life time-varying vibrations.

4.2 Powering of a Wireless Sensor Node

A robust communication network is nowadays indispensable in the transportation chain of food and medicinal products. The cold chain of perishable food requires careful monitoring of the temperature and the humidity (arising from the agri-food transpiration) when they are transported to significantly reduce food spoilage [51]. Similarly,

continuous supervision is imperative during the transportation of pharmaceuticals as the majority of drugs and vaccines lose their potency if the temperature departs from the recommended level [52]. The critical challenge is continuous in-situ monitoring of the environment when they are transported from the warehouse or manufacturer to a different distributor. This can be facilitated through a resilient self-powered wireless sensor network. The high power density VEH prototype developed in this work could be employed to power such a WSN network by harvesting energy from the vibrations of the truck that carries the product. Magnuson et al. [53] reported the vibrations recorded from a loaded truck driven on highways and the vibration in the vertical direction was found to be spread over a broadband of 40Hz to 180Hz with peak amplitudes less than 1g. This is suitable for driving the intrinsically broadband VEH fabricated in this work.

In order to power the wireless sensor nodes perpetually through vibration energy harvesting, the essential requirement is effective mechanical energy tapping along with efficient energy conversion and distribution. The power demand varies for different sensors and their associated electronics, accordingly the power conditioning circuitry connecting the source to the target node changes. In this work, we have selected the Cypress IoT kit (S6SAE101A00SA1002) which comes with Bluetooth-Low-Energy (BLE) wireless connectivity. It consists of an energy harvesting motherboard containing mainly the Power Management IC S6AE101A, Temperature and Humidity Sensor (Si7020-A10) and CYBLE-022001-00 EZ BLE. The other part of the kit is a PC compatible BLE-USB Bridge accommodating the CYBL 10162-56LQXI PRoC BLE device and a wiggle antenna along with antenna matching network. While this kit is specifically designed to scavenge photovoltaic energy or to run on a coin-cell primary battery (3V DC), but the ultra-low-power start-up of the PMIC (250nA current consumption and 1.2µW power for start-up) makes it an attractive choice to be used with vibrational energy harvesters. Typically, the motherboard requires 3.3V DC to operate and communicate the acquired data through Bluetooth connectivity. The wireless sensor node transmits the gathered data at 6 second intervals.

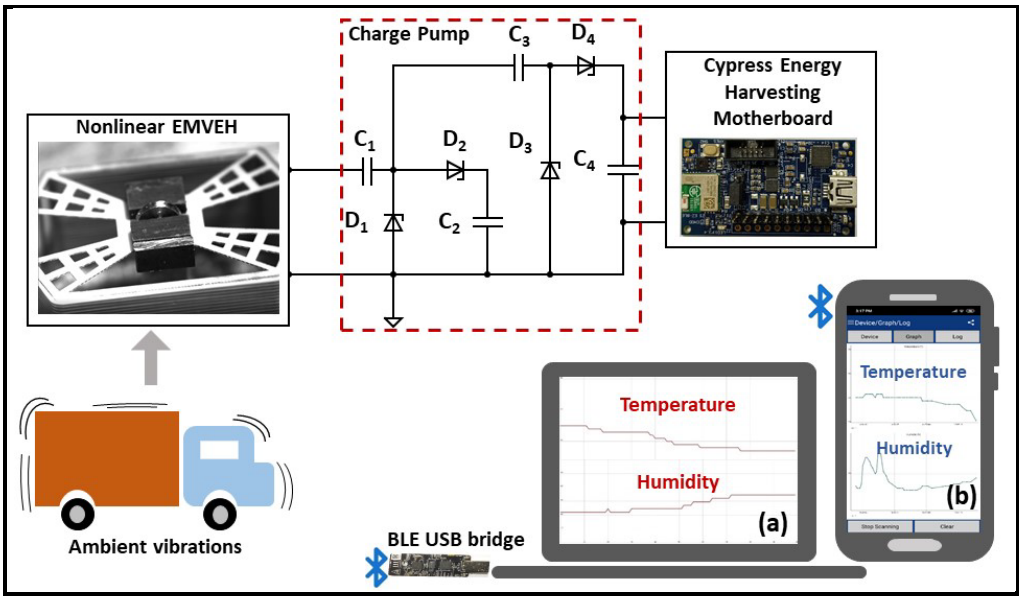

Figure 13: Overview of the energy harvesting system powering the Cypress IoT kit, (a) Logged data in the PC through wireless communication established by the BLE USB bridge (b) Logged data in the smart phone through CYPRESS BLE Beacon app when the motherboard is configured as a stand-alone wireless sensor node and it communicates through wireless bluetooth connectivity.

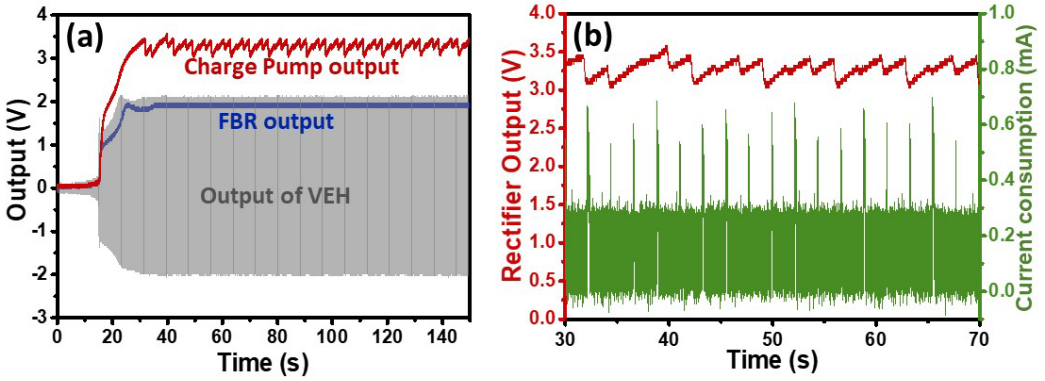

Figure 14: (a) Output voltage of the vibration energy harvester, full bridge rectifier and the charge pump circuit connected across the harvester in grey, blue and red respectively. (b) Output voltage of the charge pump circuit attached across the harvester and the current consumption of the motherboard associated with the IoT kit.

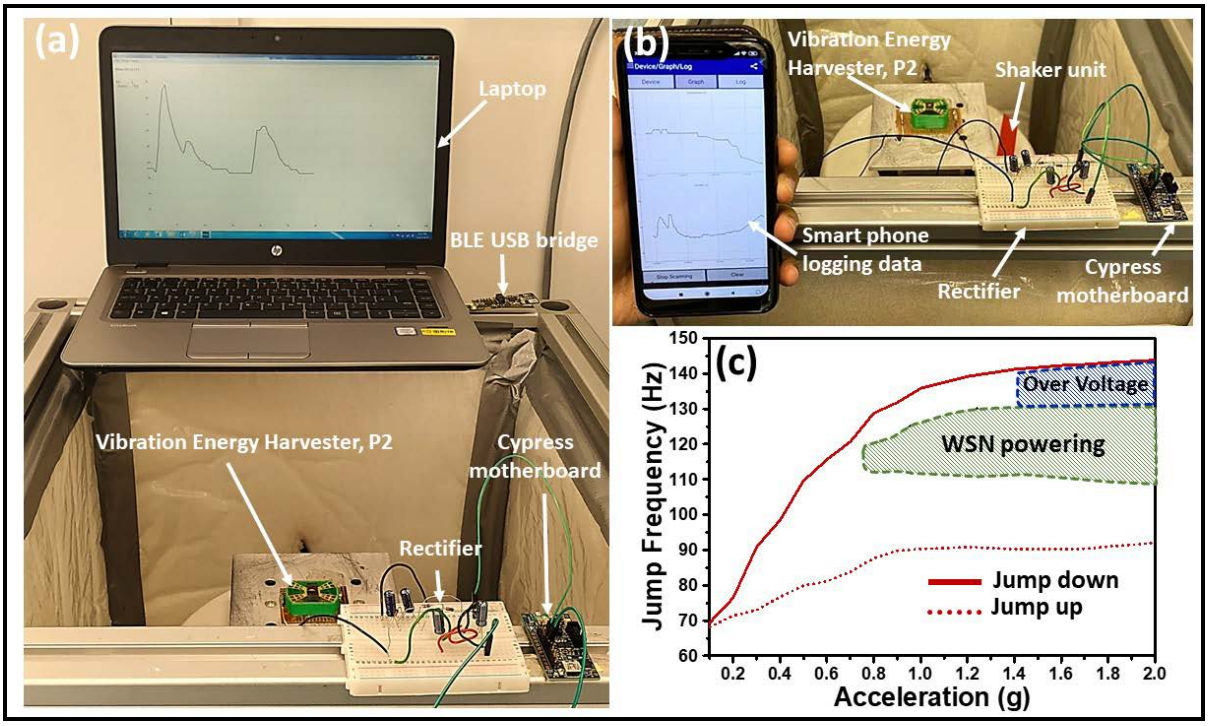

Figure 15: Depiction of the energy harvesting system with the target sensor node, (a)logging sensor data in laptop through the BLE USB bridge, (b)logging data directly in smart phone through bluetooth connectivity. (c) Illustration of the operable range of frequency and acceleration where the wireless sensor node could be powered by P2.

Throughout our study, we can clearly observe that P2 is superior in performance to P1, which is why we have chosen P2 prototype to power the target sensor node (Fig. 13). The interfacing circuitry between the harvester and the motherboard should provide a steady DC voltage of 3.3V to the motherboard. Hence, a charge-pump type rectification interface has been implemented in this case consisting of capacitors C_1 to C_4 each of 1μF and four Zener diodes D_1 to D_4 to enhance the output of the harvester unit from 2V to 3.8V DC voltage (when the harvester is driven with harmonic excitation at 0.7g, and the frequency is ramped up from 70Hz to 108Hz at a 1Hz/sec sweep rate). The charge pump circuit delivers the power to the load by the charging and discharging of the associated capacitors, functioning as a switching regulator. This particular rectification strategy is appropriate for the low current demanding target

applications. Fig. 14(a) shows a comparison of rectified voltage produced by the charge-pump rectifier (in red) with a full bridge rectifier (in blue). The voltage drop across the diodes of the full bridge rectifier restricts the output whereas the charge pump circuit enhances the output from 2V to 3.8V, which is sufficient to power the subsequent load. The stable DC output from this interface is provided to the IoT kit motherboard through the dedicated pins. On receiving sufficient power from the source, the PMIC starts charging an integrated output capacitor, further depending on the internal switching and the level of voltage in the capacitor, the stored power gets delivered to the load.

The BLE beacon of the IoT kit broadcasts 30 bytes of information periodically once it gets sufficient energy to initiate the operation. The associated communication protocol allows the kit to read data from the humidity and temperature sensor, which is then transmitted as a part of the advertisement packet. The ripples in the output of the rectifier as shown in the Fig.14 correspond to the point where the transmitter on the motherboard establishes communication with the receiver and transmits the gathered data. The current intake of the motherboard shows peaks of 0.7mA for the transmission of information that correspond to the dip in these ripples. The motherboard establishes BLE connection with a PC through the BLE USB bridge which is programmed with initial firmware that aids it to log the data from the sensors and display on the PC screen (Fig. 15(a)). This enables the user to monitor the real-time data from dedicated sensors through smart phones. The embedded bluetooth in these phone establishes communication with the motherboard and through a compatible mobile app (e.g. CYPRESS BLE Beacon used in this case). The raw received data is processed and displayed on the phone screen (Fig.15(b)).

Fig. 15(c) shows the operable range of frequencies of P2 when it is subjected to the varying amplitude of excitation. As shown previously in Fig. 7, on increasing the acceleration of excitation, the hysteresis width of the harvester unit enhances, and that is shown by the area shaded with red. From 115Hz at 0.7g acceleration P2 supplies adequate power to the Cypress IoT kit so that it transmits the sensor data. The area shaded in green in Fig. 15(c) shows the range of acceleration and frequency that is suitable for operating this wireless sensor node with P2. The energy lost in the rectification stage has caused the harvester's response to fall off the high energy branch earlier in the low to moderate level of acceleration (up to 1.2g). Beyond this, the voltage delivered by the source to the IoT kit goes beyond the safe limit of operation (2-5.5V). This region is shaded in blue as the overvoltage zone.

In the experiments so far, we only studied harmonic excitations, however in reality non-harmonic or in other words random excitations are often found. In order to test the practical applicability of the vibration energy harvester unit, it has been subjected to the random excitation imparted by a car in motion. The harvester unit has been mounted on the rear part of a Honda Civic car and it is connected to the wireless sensor platform through a rectifier circuit. A slamstick [54], which is a vibration data logger, has been used here to record the vibrations of the car (Fig. 16(b)). When the car was in motion, the harvester started powering the sensor node (Cypress IoT kit), and through the CYPRESS BLE Beacon mobile app the raw data was received in a smart phone. The data packets were received at an irregular interval, unlike the case when the harvester was subjected to harmonic excitation, reporting a temperature of 24.5˚C and 74% humidity (inside the car). Fig. 16(a) shows a snippet of the time trace of the vibrations experienced in the car. The inset shows the frequency range over which substantial mechanical energy was found to be distributed, having peaks over 12Hz, 50Hz, 71Hz and 93Hz. We received data packets over the shown time range, in Fig. 16(c) we further show the number of data packets received per second over that time frame. It is noticeable that few of the data packets were received when the vibrations had spikes, as marked with red arrows in Fig. 16(c), which may correspond to the bumps in the road. Similar spikes can be seen at the time instants marked with black arrow, however, no successful reception of data packets could be observed here. This may be attributed to the fact that although the amplitude of acceleration at this peak is as high as 0.9g to 1.2g, but the corresponding frequency component may not fall into the bandwidth over which it is possible to excite the device and extract substantial mechanical energy through it.

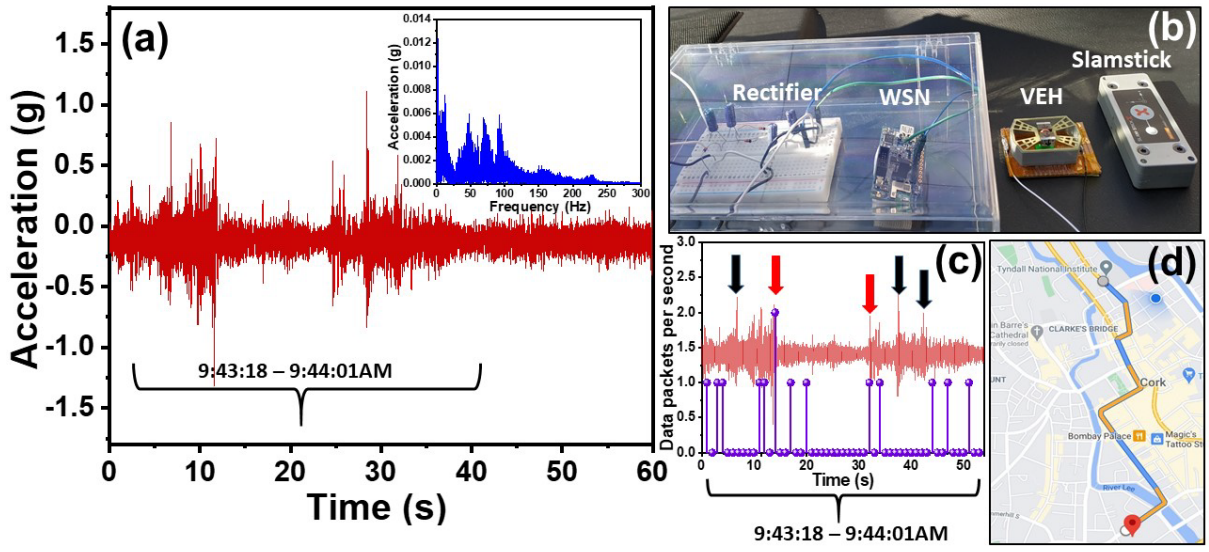

Figure 16: (a) Time trace of the vibration experienced in the rear part of a car recorded with data logger (Slamtick), the inset shows the frequency range over which substantial mechanical energy was found to be distributed in the car. (b) shows the experimental set-up consisting of the rectifier, sensor node, the energy harvester unit and a slamstick (vibration data logger) to record the vibrations from the car. (c) illustrates the number of data packets received over a small snippet of time and (d) shows the path that the car traversed around Tyndall National Institute.

The performance of the harvester unit could be further enhanced by optimizing the spring geometry. This would yield higher power at an even lower level of external excitation which along with wider operable bandwidth. These improvements could open up the possibility of using such harvester to power the network of WSNs for a wide range of applications.

Conclusion:

This work demonstrates the implementation of tapered FR4 (Flame Retardant 4) based spring architecture in an electromagnetic Vibration Energy Harvester (VEH). This harvester exhibits spring hardening nonlinearity based on large deformations, with a relatively small footprint. The atypical stress distribution of the tapered thin spring structure has been exploited to obtain a suitable nonlinearity. Through detailed experimental investigation, we have showed the efficacy of using these energy harvester prototypes to yield a power density as high as 2660$\mu W/cm^3g^2$, outpacing many of the contemporary reported devices. The inclusion of strong nonlinearity in this system resulted in an enhanced bandwidth of 45Hz at 1g acceleration which makes it suitable for extracting mechanical energy from real-world wideband vibration spectrum. Furthermore, we provided a thorough analysis of the variation of the maximum power point and also proposed a modified Perturb and Observe strategy for tracking the maximum power point in order to optimize the extractable electrical power. The fabricated energy harvester unit is also used to address the issue of providing continuous power to wireless sensor networks. This is challenging for a non-resonant VEH because of the requirement of a steady 3-3.3V DC supply to power the integrated electronics associated with a wireless sensor node. Despite this challenge, our prototype has powered such a wireless sensor node (using a Cypress IoT kit) consisting of a temperature and humidity sensor. The transmitted data is logged in a PC and smartphone through well-established Bluetooth connectivity. This makes the energy harvester a potential candidate for establishing a battery-less wireless sensor network in a wide range of application, including the food and pharmaceutical transportation chain ensuring enhanced quality and safety of the valuable products in this chain.

Acknowledgements
The authors would like to thank Dr. Dhiman Mallick and Dinesh R. Gawade for the valuable discussions and suggestions regarding this work. We would also like to thank Julie Donnelly and Philip Murphy for proof reading the presented manuscript This work is financially supported by a research grant from Science Foundation Ireland (SFI) and is co-funded under the European Regional Development Fund Grant Number 13/RC/2077. This is also part funded by the EU-H-2020 project 'Enables', Project ID: 730957.

References

[1] P. Gope and T. Hwang, "BSN-Care: A Secure IoT-Based Modern Healthcare System Using Body Sensor Network," *IEEE Sensors Journal*, vol. 16, no. 5, pp. 1368-1376, 2016, doi: 10.1109/JSEN.2015.2502401.

[2] W. He, G. Yan, and L. D. Xu, "Developing Vehicular Data Cloud Services in the IoT Environment," *IEEE Transactions on Industrial Informatics*, vol. 10, no. 2, pp. 1587-1595, 2014, doi: 10.1109/TII.2014.2299233.

[3] M. A. Mahmud, K. Bates, T. Wood, A. Abdelgawad, and K. Yelamarthi, "A complete Internet of Things (IoT) platform for Structural Health Monitoring (SHM)," in *2018 IEEE 4th World Forum on Internet of Things (WF-IoT)*, 5-8 Feb. 2018 2018, pp. 275-279, doi: 10.1109/WF-IoT.2018.8355094. [Online]. Available:https://ieeexplore.ieee.org/ielx7/8353083/8355082/08355094.pdf?tp=&arnumber=8355094&isnumber=8355082&ref

[4] J. Shah and B. Mishra, "IoT enabled environmental monitoring system for smart cities," in *2016 International Conference on Internet of Things and Applications (IOTA)*, 22-24 Jan. 2016 2016, pp. 383-388, doi:10.1109/IOTA.2016.7562757.[Online].Available:https://ieeexplore.ieee.org/ielx7/7560575/7562684/07562757.pdf?tp=&arnumber=7562757&isnumber=7562684&ref

[5] N. H. Motlagh, M. Bagaa, and T. Taleb, "UAV-Based IoT Platform: A Crowd Surveillance Use Case," *IEEE Communications Magazine*, vol. 55, no. 2, pp. 128-134, 2017, doi: 10.1109/MCOM.2017.1600587CM.

[6] J. P. Amaro, R. Cortesão, J. Landeck, and F. J. T. E. Ferreira, "Harvested Power Wireless Sensor Network Solution for Disaggregated Current Estimation in Large Buildings," *IEEE Transactions on Instrumentation and Measurement*, vol. 64, no. 7, pp. 1847-1857, 2015, doi: 10.1109/TIM.2014.2383052.

[7] Y. Lu, E. O'Riordan, F. Cottone, S. Boisseau, D. Galayko, E. Blokhina *et al.*, "A batch-fabricated electret-biased wideband MEMS vibration energy harvester with frequency-up conversion behavior powering a UHF wireless sensor node," *Journal of Micromechanics and Microengineering*, vol. 26, no. 12, p. 124004, 2016/09/29 2016, doi: 10.1088/0960-1317/26/12/124004.

[8] L. Wang, G. Luo, Z. Jiang, F. Zhang, L. Zhao, P. Yang *et al*., "Broadband vibration energy harvesting for wireless sensor node power supply in train container," *Review of Scientific Instruments*, vol. 90, no. 12, p. 125003, 2019/12/01 2019, doi: 10.1063/1.5127243.

[9] W. Hwang, K. B. Kim, J. Y. Cho, C. H. Yang, J. H. Kim, G. J. Song *et al*., "Watts-level road-compatible piezoelectric energy harvester for a self-powered temperature monitoring system on an actual roadway," *Applied Energy*, vol. 243, pp. 313-320, 2019/06/01/ 2019, doi: https://doi.org/10.1016/j.apenergy.2019.03.122.

[10] S. P. Beeby, R. N. Torah, M. J. Tudor, P. Glynne-Jones, T, O'Donnel, C. R. Saha et al., "A micro electromagnetic generator for vibration energy harvesting," *Journal of Micromechanics and Microengineering*, vol. 17, no. 7, pp. 1257-1265, 2007/06/05 2007, doi: 10.1088/0960-1317/17/7/007.

[11] S. H. Chae, S. Ju, Y. Choi, Y.-E. Chi, and C.-H. Ji, "Electromagnetic Linear Vibration Energy Harvester Using Sliding Permanent Magnet Array and Ferrofluid as a Lubricant," (in eng), *Micromachines (Basel)*, vol. 8, no. 10, p. 288, 2017, doi: 10.3390/mi8100288.

[12] I.-H. Kim, H.-J. Jung, B. M. Lee, and S.-J. Jang, "Broadband energy-harvesting using a two degree-of-freedom vibrating body," *Applied Physics Letters*, vol. 98, no. 21, p. 214102, 2011/05/23 2011, doi: 10.1063/1.3595278.

[13] H.-C. Song, P. Kumar, R. Sriramdas, H. Lee, N. Sharpes, M.-G. Kang *et al.*, "Broadband dual phase energy harvester: Vibration and magnetic field," *Applied Energy*, vol. 225, pp. 1132-1142, 2018/09/01/ 2018, doi:https://doi.org/10.1016/j.apenergy.2018.04.054.

[14] V. R. Challa, M. G. Prasad, Y. Shi, and F. T. Fisher, "A vibration energy harvesting device with bidirectional resonance frequency tunability," *Smart Materials and Structures*, vol. 17, no. 1, p. 015035, 2008/01/08 2008, doi: 10.1088/0964-1726/17/01/015035.

[15] L. Zhao and Y. Yang, "An impact-based broadband aeroelastic energy harvester for concurrent wind and base vibration energy harvesting," *Applied Energy*, vol. 212, pp. 233-243, 2018/02/15/ 2018, doi: https://doi.org/10.1016/j.apenergy.2017.12.042.

[16] X. Wang, C. Chen, N. Wang, H. San, Y. Yu, E. E. Halvorsen *et al.*, "A frequency and bandwidth tunable piezoelectric vibration energy harvester using multiple nonlinear techniques," *Applied Energy*, vol. 190, pp. 368-375, 2017/03/15/ 2017, doi: https://doi.org/10.1016/j.apenergy.2016.12.168.

[17] P. Podder, D. Mallick, A. Amann, and S. Roy, "Influence of combined fundamental potentials in a nonlinear vibration energy harvester," *Scientific Reports*, Article vol. 6, p. 37292, 11/22/online 2016, doi: 10.1038/srep37292.

[18] S. Roy, P. Podder, and D. Mallick, "Nonlinear Energy Harvesting Using Electromagnetic Transduction for Wide Bandwidth," *IEEE Magnetics Letters*, vol. 7, pp. 1-4, 2016, doi: 10.1109/LMAG.2015.2509938.

[19] B. Marinkovic and H. Koser, "Smart Sand—A Wide Bandwidth Vibration Energy Harvesting Platform," *Applied Physics Letters - APPL PHYS LETT*, vol. 94, 03/09 2009, doi: 10.1063/1.3097207.

[20] D. Mallick, A. Amann, and S. Roy, "A nonlinear stretching based electromagnetic energy harvester on FR4 for wideband operation," *Smart Materials and Structures*, vol. 24, no. 1, p. 015013, 2014/11/27 2014, doi: 10.1088/0964-1726/24/1/015013.

[21] B. P. Mann and N. D. Sims, "Energy harvesting from the nonlinear oscillations of magnetic levitation," *Journal of Sound and Vibration*, vol. 319, no. 1, pp. 515-530, 2009/01/09/ 2009, doi: https://doi.org/10.1016/j.jsv.2008.06.011.

[22] P. Constantinou and S. Roy, "A 3D printed electromagnetic nonlinear vibration energy harvester," *Smart Materials and Structures*, vol. 25, no. 9, p. 095053, 2016/08/24 2016, doi: 10.1088/0964-1726/25/9/095053.

[23] F. Cottone, H. Vocca, and L. Gammaitoni, "Nonlinear Energy Harvesting," *Physical Review Letters*, vol. 102, no. 8, p. 080601, 02/23/ 2009, doi: 10.1103/PhysRevLett.102.080601.

[24] A. Erturk and D. J. Inman, "Broadband piezoelectric power generation on high-energy orbits of the bistable Duffing oscillator with electromechanical coupling," *Journal of Sound and Vibration*, vol. 330, no. 10, pp. 2339-2353, 2011/05/09/ 2011, doi: https://doi.org/10.1016/j.jsv.2010.11.018.

[25] P. Podder, A. Amann, and S. Roy, "A bistable electromagnetic micro-power generator using FR4-based folded arm cantilever," *Sensors and Actuators A: Physical*, vol. 227, pp. 39-47, 2015/05/15/ 2015, doi: https://doi.org/10.1016/j.sna.2015.03.043.

[26] P. Podder, A. Amann, and S. Roy, "Combined Effect of Bistability and Mechanical Impact on the Performance of a Nonlinear Electromagnetic Vibration Energy Harvester," *IEEE/ASME Transactions on Mechatronics*, vol. 21, no. 2, pp. 727-739, 2016, doi: 10.1109/TMECH.2015.2451016.

[27] S. Zhao and A. Erturk, "On the stochastic excitation of monostable and bistable electroelastic power generators: Relative advantages and tradeoffs in a physical system," *Applied Physics Letters*, vol. 102, no. 10, p. 103902, 2013/03/11 2013, doi: 10.1063/1.4795296.

[28] D. Mallick, A. Amann, and S. Roy, "Surfing the High Energy Output Branch of Nonlinear Energy Harvesters," *Physical Review Letters*, vol. 117, no. 19, p. 197701, 11/04/ 2016, doi: 10.1103/PhysRevLett.117.197701.

[29] G. Aldawood, H. T. Nguyen, and H. Bardaweel, "High power density spring-assisted nonlinear electromagnetic vibration energy harvester for low base-accelerations," *Applied Energy*, vol. 253, p. 113546, 2019/11/01/ 2019, doi: https://doi.org/10.1016/j.apenergy.2019.113546.

[30] K. Fan, Q. Tan, Y. Zhang, S. Liu, M. Cai, and Y. Zhu, "A monostable piezoelectric energy harvester for broadband low-level excitations," *Applied Physics Letters*, vol. 112, no. 12, p. 123901, 2018/03/19 2018, doi: 10.1063/1.5022599.

[31] A. Vyas, H. Staaf, C. Rusu, T. Ebefors, J. Lijeholm, A. D. Smith *et al.*, "A Micromachined Coupled Cantilever for Piezoelectric Energy Harvesters," (in eng), *Micromachines (Basel)*, vol. 9, no. 5, p. 252, 2018, doi: 10.3390/mi9050252.

[32] H. Salmani, G. H. Rahimi, and S. A. Hosseini Kordkheili, "An Exact Analytical Solution to Exponentially Tapered Piezoelectric Energy Harvester," *Shock and Vibration*, vol. 2015, p. 13, 2015, Art no. 426876, doi: 10.1155/2015/426876.

[33] S. Paquin and Y. St-Amant, "Improving the performance of a piezoelectric energy harvester using a variable thickness beam," *Smart Materials and Structures*, vol. 19, no. 10, p. 105020, 2010/08/18 2010, doi: 10.1088/0964-1726/19/10/105020.

[34] I. Guzelbey, Y. Eraslan, and M. Doğru, "Effects of Taper Ratio on Aircraft Wing Aerodynamic Parameters: A Comperative Study," 03/20 2019, doi: 10.26701/ems.487516.

[35] S. Roundy, P. Wright, and J. M. Rabaey, "A Study of Low Level Vibrations as a Power Source for Wireless Sensor Nodes," *Computer Communications*, vol. 26, pp. 1131-1144, 07/01 2003, doi: 10.1016/S0140-3664(02)00248-7.

[36] R. L. Harne and K. W. Wang, "A review of the recent research on vibration energy harvesting via bistable systems," *Smart Materials and Structures*, vol. 22, no. 2, p. 023001, 2013/01/28 2013, doi: 10.1088/0964-1726/22/2/023001.

[37] T. Zhang, H. G. Li, and Y. Bi, "Hysteresis characteristics influence on the super-harmonic vibration of a bi-stable piezoelectric energy harvester," *Journal of Low Frequency Noise, Vibration and Active Control*, vol. 37, no. 4, pp. 1003-1014, 2018/12/01 2018, doi: 10.1177/1461348418784190.

[38] R. Masana and M. F. Daqaq, "Energy harvesting in the super-harmonic frequency region of a twin-well oscillator," *Journal of Applied Physics*, vol. 111, no. 4, p. 044501, 2012/02/15 2012, doi: 10.1063/1.3684579.

[39] D. Mallick and S. Roy, "Bidirectional electrical tuning of FR4 based electromagnetic energy harvesters," *Sensors and Actuators A: Physical*, vol. 226, pp. 154-162, 2015/05/01/ 2015, doi: https://doi.org/10.1016/j.sna.2015.02.016.

[40] C. R. Saha, T. O. Donnell, H. Loder, S. Beeby, and J. Tudor, "Optimization of an Electromagnetic Energy Harvesting Device," *IEEE Transactions on Magnetics*, vol. 42, no. 10, pp. 3509-3511, 2006, doi: 10.1109/TMAG.2006.879447.

[41] M. J. Brennan, I. Kovacic, A. Carrella, and T. P. Waters, "On the jump-up and jump-down frequencies of the Duffing oscillator," *Journal of Sound and Vibration*, vol. 318, no. 4, pp. 1250-1261, 2008/12/23/ 2008, doi: https://doi.org/10.1016/j.jsv.2008.04.032.

[42] D. Maurath, P. F. Becker, D. Spreemann, and Y. Manoli, "Efficient Energy Harvesting With Electromagnetic Energy Transducers Using Active Low-Voltage Rectification and Maximum Power Point Tracking," *IEEE Journal of Solid-State Circuits*, vol. 47, no. 6, pp. 1369-1380, 2012, doi: 10.1109/JSSC.2012.2188562.

[43] C. Lu, C. Tsui, and W. Ki, "Vibration Energy Scavenging System With Maximum Power Tracking for Micropower Applications," *IEEE Transactions on Very Large Scale Integration (VLSI) Systems*, vol. 19, no. 11, pp. 2109-2119, 2011, doi: 10.1109/TVLSI.2010.2069574.

[44] A. Reza Reisi, M. Hassan Moradi, and S. Jamasb, "Classification and comparison of maximum power point tracking techniques for photovoltaic system: A review," *Renewable and Sustainable Energy Reviews*, vol. 19, pp. 433-443, 2013/03/01/ 2013, doi: https://doi.org/10.1016/j.rser.2012.11.052.

[45] R. Bradai, R. Boukenoui, A. Kheldoun, H. Salhi, M. Ghanes, J-P. Barbot *et al.*, "Experimental assessment of new fast MPPT algorithm for PV systems under non uniform irradiance conditions," *applied energy*, vol. 199, pp. 416-429, 08/01 2017, doi: 10.1016/j.apenergy.2017.05.045.

[46] A. Belkaid, I. Colak, and O. Isik, "Photovoltaic maximum power point tracking under fast varying of solar radiation," *Applied Energy*, vol. 179, pp. 523-530, 2016/10/01/ 2016, doi: https://doi.org/10.1016/j.apenergy.2016.07.034.

[47] L. Costanzo and M. Vitelli, "Resonant electromagnetic vibration harvesters applications: Optimization of P&O MPPT technique parameters," in *2018 Thirteenth International Conference on Ecological Vehicles and Renewable Energies (EVER)*, 10-12 April 2018 2018, pp. 1-8, doi: 10.1109/EVER.2018.8362384. [Online]. Available: https://ieeexplore.ieee.org/ielx7/8360088/8362327/08362384.pdf?tp=&arnumber=8362384&isnumber=8362327&ref=

[48] A. Dudka, P. Basset, F. Cottone, E. Blokhina, and D. Galayko, "Wideband Electrostatic Vibration Energy Harvester (e-VEH) Having a Low Start-Up Voltage Employing a High-Voltage Integrated Interface," *Journal of Physics: Conference Series*, vol. 476, p. 012127, 2013/12/04 2013, doi: 10.1088/1742-6596/476/1/012127.

[49] J. F. Dickson, "On-chip high-voltage generation in MNOS integrated circuits using an improved voltage multiplier technique," *IEEE Journal of Solid-State Circuits*, vol. 11, no. 3, pp. 374-378, 1976, doi: 10.1109/JSSC.1976.1050739.

[50] L. Costanzo, A. L. Schiavo, and M. Vitelli, "Design Guidelines for the Perturb and Observe Technique for Electromagnetic Vibration Energy Harvesters Feeding Bridge Rectifiers," *IEEE Transactions on Industry Applications*, vol. 55, no. 5, pp. 5089-5098, 2019, doi: 10.1109/TIA.2019.2923162.

[51] S. T. Hammond *et al.*, "Food Spoilage, Storage, and Transport: Implications for a Sustainable Future," *BioScience*, vol. 65, no. 8, pp. 758-768, 2015, doi: 10.1093/biosci/biv081.

[52] G. Haan, J. Hillegersberg, E. Jong, and K. Sikkel, "Adoption of Wireless Sensors in Supply Chains: A Process View Analysis of a Pharmaceutical Cold Chain," *Journal of theoretical and applied electronic commerce research*, vol. 8, pp. 138-154, 08/01 2013, doi: 10.4067/S0718-18762013000200011.

[53] C. F. Magnuson, L. T. Wilson, "Shock and Vibration Environments for Large Shipping Containers on Rail Cars and Trucks," *SAND76-0427, NUREG766510.* , Technical Report 1977, doi: 10.2172/7305222.

[54] Midé Slamtick, Shock and Vibration data loggers, datasheet, https://www.mouser.ie/pdfdocs/slam-stick-vibration-data-loggers-datasheet.pdf